

# **Daytime Cirrus Cloud Top-of-Atmosphere Radiative Forcing Properties at a Midlatitude Site and their Global Consequence**

**James R. Campbell\***

*Naval Research Laboratory, Monterey, California, USA*

**Simone Lolli**

*Joint Center for Earth Systems Technology*

*University of Maryland Baltimore County, Baltimore, Maryland, USA*

**Jasper R. Lewis**

*Joint Center for Earth Systems Technology*

*University of Maryland Baltimore County, Baltimore, Maryland, USA*

**Yu Gu**

*University of California Los Angeles, Los Angeles, California, USA*

**Ellsworth J. Welton**

*NASA/Goddard Space Flight Center, Greenbelt, Maryland, USA*

**Submitted to**

*Journal of Applied Meteorology and Climatology*

12 August 2015

**Revised**

1 February 2016

---

\* Corresponding author address: c/o 7 Grace Hopper Rd. Stop 2, Monterey, California, 93943. E-mail:  
james.campbell@nrlmry.navy.mil

**ABSTRACT**

One-year of continuous ground-based lidar observations (2012) are analyzed for single-layer cirrus clouds at the NASA Micro Pulse Lidar Network site at the Goddard Space Flight Center to investigate top-of-atmosphere (TOA) annual net daytime radiative forcing properties. A slight positive net daytime forcing is estimated (i.e., warming) :  $0.07 - 0.67 \text{ W/m}^2$  in relative terms, which reduces to  $0.03 - 0.27 \text{ W/m}^2$  in absolute terms after normalizing to unity based on approximated 40% midlatitude occurrence frequency rate estimated from satellite. Results are based on bookend solutions for lidar extinction-to-backscatter (20 and 30 sr) and corresponding retrievals for 532 nm cloud extinction coefficient. Uncertainties due to cloud undersampling, attenuation effects, sample selection and lidar multiple scattering are described. A net daytime cooling effect is found from the very thinnest clouds (cloud optical depth  $\leq 0.01$ ) that is attributed to relatively high solar zenith angles. A relationship between positive/negative daytime cloud forcing is demonstrated as a function of solar zenith angle and cloud top temperature. These properties, combined with the influence of varying surface albedos, are used to conceptualize how daytime cloud forcing likely varies with latitude and season, with cirrus clouds exerting less positive forcing and potentially net TOA cooling approaching the summer poles (non-ice and snow covered) versus greater warming at the equator. The existence of such a gradient would lead cirrus to induce varying daytime TOA forcing annually and seasonally, making it a far greater challenge than presently believe to constrain daytime and diurnal cirrus contributions to global radiation budgets.

22

23    **1. Background**

24    Cirrus clouds have long been recognized for their unique contribution to climate (Liou 1986).  
25    In particular, whereas all clouds warm the atmosphere at night (positive top-of-atmosphere  
26    forcing; TOA), cirrus is the only genus that can readily warm or cool (negative TOA forcing;  
27    effectively all other clouds cool the daytime atmosphere) the daytime atmosphere depending on  
28    their varying physical characteristics (i.e., cloud heights, temperatures, effective particle sizes,  
29    surface thermal contrast and ice water path/cloud optical depth; e.g., Stephens and Webster  
30    1981). Conceptual models have long been established based on episodic regional measurements  
31    or modeling case studies depicting the offsetting relationship between cirrus cloud infrared  
32    absorption and reemission and solar albedo effects (e.g., Ackerman et al. 1988; Fu et al. 1993;  
33    Jensen et al. 1994). They generally depict cirrus as daytime TOA warming agents, wherein  
34    clouds exhibiting an optical depth up to near 1.0 cause a positive net TOA forcing effect that  
35    exceeds negative net forcing (cooling) by optically-thicker clouds. Further, they imply that the  
36    most significant forcing comes from optically-thicker clouds, wherein optically-thin clouds  
37    contribute little to the overall forcing budget.

38    These classical conceptual models however, and thus the basis for our understanding of  
39    cirrus cloud forcing within the global cloud radiation budget, were built on regional or single-site  
40    datasets collected using long-antiquated remote sensing methodologies, and thus a fundamentally  
41    lesser understanding of the global variability in cirrus cloud physical properties and occurrence  
42    frequencies. With advanced ground and satellite-based observing systems established over  
43    recent years, progress is being made at refining these models and better isolating the net daytime  
44    forcing impact of cirrus clouds globally. In particular, we now recognize that cirrus clouds are  
45    the most common cloud genus observed (in terms of absolute frequencies) in the atmosphere

46 (Stubenrauch et al. 2013, *and references therein*), with global occurrence frequencies ranging  
47 from 40-60% (Mace et al., 2009). Further, cirrus skew heavily toward relatively low ice water  
48 content and low optical depth clouds (e.g., Sassen and Campbell, 2001; Holz et al. 2008; Mace et  
49 al. 2009; Campbell et al. 2015).

50 The impact of this new and evolving understanding of cirrus has recently been highlighted by  
51 Berry and Mace (2014). They consider two years of integrated NASA A-Train Cloud Profiling  
52 Radar (CPR; Stephens et al. 2003) and Cloud-Aerosol Lidar with Orthogonal Polarization  
53 (CALIOP; Winker et al. 2010) cloud measurements over Southeast Asia, deriving a  
54 climatological model for tropical cirrus diurnal net TOA cloud forcing during the regional  
55 summer monsoon period. Specifically, they recognize that net cloud forcing functions, similar to  
56 those of the classic models outlined above, must be normalized by the relative frequencies of  
57 cloud occurrence. Accordingly, this shifts the relative burden of net cirrus cloud forcing toward  
58 more diffuse clouds, which are exponentially more prevalent, yielding a far more accurate net  
59 forcing budget for that properly reconciles the climatic significance of optically-thin clouds  
60 (optical depths < 0.3; Sassen and Cho 1992) that is enhanced in the aggregate.

61 In this paper, net daytime TOA cirrus cloud forcing (CRF) is evaluated for data collected at a  
62 midlatitude site. Pairing a continuous one-year ground-based lidar-derived cirrus cloud  
63 observational dataset with a radiative transfer model, annual net daytime TOA cloud forcing  
64 characteristics are described. A slight positive annual net forcing (warming) is estimated overall.  
65 However, a net daytime cooling contribution is found from the very thinnest clouds, a discovery  
66 consistent with prior theory, and one that can be inferred from previous studies though the  
67 process has yet to be specifically distinguished. Further, a distinct relationship between the sign  
68 of net daytime forcing is resolved as a function of solar zenith angle and cloud top temperature (a

69 proxy in this context for height). These properties in tandem, combined with consideration of  
70 varying surface albedos, imply that annual net daytime cirrus cloud forcing likely varies with  
71 latitude, which in turn raises question as to how the sign and magnitude of daytime cirrus forcing  
72 may vary seasonally with latitude and what the net daytime cirrus forcing contribution to the  
73 global radiation budget is overall. These processes are described, and the means for how they  
74 interrelate and impact net daytime TOA CRF solutions globally are hypothesized. The result is a  
75 relatively simple depiction of forcing characteristics for a distinct midlatitude site overall, but  
76 more importantly a conceptual model for how variance in daytime cirrus forcing likely manifests  
77 meridionally over the global system.

78

## 79 **2. Daytime Cirrus TOA Cloud Radiative Forcing Calculations at Greenbelt, Maryland**

### 80 2.1 2012 MPLNET Cirrus Cloud Subset at Greenbelt, Maryland

81 One-year of continuous lidar-based cloud observations were collected in 2012 at the NASA  
82 Goddard Space Flight Center (GSFC) in Greenbelt, Maryland ( $38.99^{\circ}$  N,  $76.84^{\circ}$  W, 0.050 km  
83 above mean sea level; MSL) using a 532 nm NASA Micro Pulse Lidar Network<sup>1</sup> instrument  
84 (MPLNET; Welton et al. 2001; Campbell et al. 2002). Cirrus clouds were retrieved from these  
85 data using signal processing algorithms described in Campbell et al. (2008) and Lewis et al.  
86 (2016). Specifically, however, genus discrimination is based on a thermal threshold that restricts  
87 the sample to clouds with a corresponding top height temperature no warmer than  $-37^{\circ}$  C. The  
88 justification for applying this restriction with respect to MPLNET profiling is outlined in  
89 Campbell et al. (2015), based on cirrus cloud climatological properties reported by Sassen and  
90 Campbell (2001) and given the single-channel elastic backscatter signal available currently from  
91 the instrument.

---

<sup>1</sup> <http://mplnet.gsfc.nasa.gov/>

92       The daytime cirrus cloud subset analyzed here consists solely of single-layer scene clouds  
93       (i.e., only cirrus and no other clouds). This decision limits the influence of attenuation-limiting  
94       effects within the sample (i.e., in resolving cloud top and through multi-layer structures). Lewis  
95       et al. (2016) describe use of 1, 5 and 20-min sampling periods to resolve cirrus cloud presence in  
96       MPLNET products, wherein clouds are sought and distinguished at each resolution and  
97       regridded to a one-minute feature mask (1440 potential observations per day). Relatively high-  
98       resolution data sampling was thus applied for optimizing instrument signal-to-noise and retrieval  
99       performance at cirrus cloud altitudes during daylight hours (see Campbell et al. 2008 for an  
100      assessment of how MPL upper tropospheric cloud detection varies with temporal sampling  
101      resolution). One-minute sampling was applied here at a nearly 3-to-1 rate more than the longer  
102      averages combined. A total of 21,107 single cirrus cloud layers were compiled and studied.

103       Daytime is designated in this study as being those hours when incoming clear-sky net solar  
104       radiance exceeds net outgoing energy. This condition limits apparent daylight hours versus those  
105       found with a more traditional definition based on solar zenith angle (SZA) relative to the horizon  
106       alone. Instead, this is an approximate threshold that segregates the diurnal cycle by contrasting  
107       periods where net TOA CRF can be both positive or negative (daytime) versus those where it can  
108       only be positive (nighttime; the impact of this decision within the analysis will be more clearly  
109       apparent in Sec. 2.4). Note that the true threshold separating such daily periods is always  
110       slightly lower with respect to incoming solar radiance in the presence of cloud than that applied,  
111       depending on SZA, cloud physical properties and thermal surface contrast. For practical  
112       purposes here, though, these differences are inconsequential. The distinction is critical, however,  
113       for isolating the sign and corresponding magnitude of relative net daytime TOA CRF. The

114 relative distribution of daytime to nighttime hours in this year-long analysis is approximately 40-  
115 to-60%.

116 The 532 nm cloud extinction coefficient is the primary dependent lidar variable used to  
117 simulate cloud radiative properties (Sec. 2.2). MPLNET/single-channel elastic lidar solutions for  
118 cirrus cloud extinction coefficient, however, are unconstrained (i.e., Fernald 1984), meaning that  
119 they cannot be solved directly. Therefore, the parameter is retrieved simultaneously here using  
120 both 20 and 30 sr values for the extinction-to-backscatter ratio (the so-called “lidar ratio”),  
121 respectively (e.g., Garnier et al. 2015), to directly solve the lidar equation and resolve “bookend”  
122 variance within the applied retrievals (see Chew et al. 2011 for a similar instance where such  
123 bookend lidar ratio solutions are applied to estimate practical variance in MPLNET cirrus cloud  
124 extinction coefficient and optical depth analyses). The two values are chosen broadly so as to  
125 account both for lidar ratio variability itself and for variance arising from subsequent system  
126 uncertainties introduced in the following discussion.

127 Multiple scattering is not considered in the solutions here for lidar extinction and cloud  
128 optical depth (COD). MPLNET instruments feature an unusually low field-of-view that  
129 generally suppresses the effects of multiple scattering. However, the presence of relatively large  
130 cirrus ice crystals corresponds with increasingly-focused forward scattering of the laser along the  
131 forward-propagating plane, and thus the effect may become significant for portions of the cloud  
132 sample. MPLNET instruments have never been quantitatively evaluated for multiple scattering  
133 effects from clouds. Campbell et al. (2001) report an MPL field-of-view near 100  $\mu\text{rad}$ .  
134 Estimates from Donovan and van Lammeren (2001) indicate that the impact for instruments  
135 featuring similar fields-of-view could be overestimates of total extinction and COD approaching  
136 10%. However, the 100  $\mu\text{rad}$  value has significantly decreased (by greater than 10%) in current

137 MPLNET instruments, having integrated a more rugged and athermal telescope design that  
138 features a longer focal length than the original systems. It is therefore unclear how any such  
139 modeling estimates of multiple scattering practically relate to current versions of the technology.

140 Shown in Fig. 1 are probability distribution functions (PDFs) for frequencies of daytime  
141 cirrus cloud top height altitude, depth and top height temperature from the 2012 GSFC sample,  
142 broken down into respective sub-samples for COD solved using both 20 and 30 sr. Cloud tops  
143 vary in altitude between 6.0 and 16.0 km MSL, in cloud depth between 0.0 and 5.0 km and for  
144 cloud top temperatures  $\leq -37^{\circ}$  C. The relative frequency of cirrus observed during day versus  
145 night in the sample is almost exactly 40-vs-60%, implying no day/night data sampling bias  
146 present given those constraints introduced above. The sample is weighted decidedly, however,  
147 toward diffuse clouds. 32%/24% of the cloud samples correspond with sub-visual cirrus ( $COD \leq$   
148 0.03; cloud optical categories follow the classification rubric of Sassen and Cho 1992), at 20/30  
149 sr respectively. Accordingly, the higher extinction-to-backscatter value corresponds with greater  
150 COD, and the relative distribution shifts within each sub-sample. 47%/42% correspond with  
151 optically-thin cirrus ( $0.03 < COD \leq 0.30$ ), and 21%/34% of the samples reflect relatively opaque  
152 clouds with  $COD > 0.30$ .

153 Sampling bias at cirrus cloud altitudes is inherent to ground-based lidar observation due to  
154 signal attenuation from low-level liquid water clouds and through optically-thick cirrus. Despite  
155 a reasonable and consistent set of sample constraints introduced above, for instance, attenuation  
156 effects can never be fully suppressed with respect to profiling above an initial cloud base. The  
157 result is that some clouds are reported with a relatively low-biased cloud top, and thus a  
158 truncated extinction coefficient profile and low-biased COD estimate, and others are not  
159 identified at all within multi-layer scenes. Sassen and Cho (1992) suggest that COD values

160 between 3 and 5 reflect a practical upper limit for lidar cloud profiling due to increasing signal  
161 attenuation effects. Campbell et al. (2015) show that this value is likely closer to 2.4 in current  
162 Version 3 CALIOP datasets. COD estimates up to 3.0 are included in the 30 sr sample, as  
163 described above.

164 The lack of multi-layer cirrus and liquid-water cloud scenes within the sample introduces an  
165 additional measure of sampling bias toward optically-thinner clouds relative to attenuation  
166 effects alone. Such cases presumably tend toward higher COD. As a whole, the absolute  
167 daytime cirrus cloud frequency at GSFC within the sample is 16%, which is low by at least a  
168 factor of two relative to CALIOP observations in the midlatitudes (e.g., Mace et al. 2009). Of  
169 those clouds profiled, however, relative frequencies of thinner clouds within the sample are  
170 significantly higher than previous midlatitude estimates (80%/65% of clouds with optical depths  
171  $\leq 0.30$  at 20/30 sr, respectively, versus  $\sim 50\%$  found by Sassen and Campbell, 2001), thus very  
172 likely reflecting a disproportionate lack of relatively thicker clouds overall.

173 Thorsen et al. (2011) and Protat et al. (2014) describe sensitivities to cirrus cloud physical  
174 properties, relative frequencies of occurrence and radiative characteristics derived from ground-  
175 based lidar and radar measurements, including MPLs operated by the United States Department  
176 of Energy, versus satellite-based profiling by CPR and CALIOP. Satellite sampling, and thus  
177 nadir-pointing profiling, overcomes many ground-based limitations, though it is by no means  
178 bias free either. CALIOP profiles the earth in a sun-synchronous orbital track, which inhibits  
179 daily diurnal cloud profiling at a single site, or potentially region, equally leading to  
180 unrepresentative sample datasets in their own right, particularly with respect to the focus of the  
181 current study. Reconciliation of corresponding ground-based and satellite studies, though  
182 relatively nascent, is a critical line of inquiry.

183

184      2.2 Radiative Transfer Modeling System

185      All cloudy and clear-sky contextual radiances considered here were solved using the Fu-  
186      Liou-Gu (FLG) radiative transfer model (Fu and Liou 1992; 1993; Gu et al. 2003; Gu et al.  
187      2011). FLG is a combination of the delta-four-stream approximation for solar flux calculations  
188      [Liou et al. 1988] and delta-two/four-stream approximation for IR flux calculations [Fu et al.  
189      1997], which are divided into six and twelve bands respectively. The delta-two/four-stream  
190      combination method is sufficiently economical for IR calculations (four times faster than delta-  
191      four-stream, but only 50% more than two-stream), and at the same time it produces acceptable  
192      accuracy under most atmospheric conditions. The  $K$ -distribution method is used to parameterize  
193      non-gray gaseous absorption by CH<sub>4</sub>, O<sub>3</sub>, CO<sub>2</sub> and H<sub>2</sub>O.

194      Cirrus cloud single-scattering properties in FLG are parameterized in terms of ice water  
195      content and mean effective ice crystal diameter based on Liou et al. (2008; Sec. 3), repeated in  
196      Gu et al. (2011; Eqns. 1-3), with corresponding numerical coefficients determined from the  
197      scattering and absorption database compiled and reported by Yang et al. (2000) for the solar  
198      spectrum and Yang et al. (2005) for the infrared. The model assumes a mixed distribution of  
199      randomly-oriented ice crystal shapes, consisting of 50% bullet rosettes, 30% columns and 20%  
200      plates. Effective mean particle diameter and ice water content are solved with empirical  
201      formulae built specially into FLG for this experiment (Eqns. 9e from Heymsfield et al. 2014).  
202      Effective mean particle diameter at each lidar range bin is solved based on the cloud temperature  
203      profile, derived for each case from Goddard Earth Observing System Model Version 5.9.1<sup>2</sup>  
204      (GEOS-5) meteorological reanalysis data. The MPLNET-derived extinction coefficient is then  
205      paired with effective mean particle diameter to solve ice water content at each corresponding bin.

---

<sup>2</sup> <http://gmao.gsfc.nasa.gov/products>

206 Surface albedo values used in the model are monthly-averaged broadband estimates based on  
207 MODerate Resolution Infrared Spectroradiometer (MODIS) measurements of integrated  
208 directional hemispherical reflectance near the GSFC site (black-sky albedo; Strahler et al. 1999).  
209 Values of broadband surface albedo range between 0.12 and 0.15 annually. An 11  $\mu\text{m}$  land-  
210 surface emissivity value of 0.97 is used, based on Jin and Liang (2006). A summary of all  
211 relevant model and input sample parameters relevant to the experimental design, and introduced  
212 to this point, is outlined in Table 1.

213

214 2.3 Top-of-Atmosphere Daytime Cirrus Cloud Forcing Properties and Uncertainties

215 Figure 2a depicts the average daytime shortwave (SW), infrared (IR) and net daytime TOA  
216 CRF (defined as the difference in outgoing net TOA radiance in clear sky versus that for a given  
217 cloud, using a common thermodynamic profile) at both 20 and 30 sr as a function of COD in  
218 0.03 resolution intervals between 0.00 and 3.00. These functions are expanded upon in scale in  
219 Fig. 2b, shown again at both 20 and 30 sr now as a function of COD in 0.01 resolution intervals  
220 between 0.00 and 0.10. Since a consistent cloud sample is used for both the 20 and 30 sr  
221 solutions, and considering the analysis in Fig. 2a extends to COD = 3.00, this causes the  
222 maximum corresponding COD resolved at 20 sr to occur at only 0.73. Hence, this is why that  
223 function extends only to near that value, and why noise in that solution is apparent past about  
224 0.70. Maximum net forcing is 3.78 and 5.71  $\text{W}/\text{m}^2$ , respectively, at 20 and 30 sr, corresponding  
225 with 0.21 and 0.24 COD values. The primary crossover points between positive and negative net  
226 daytime TOA CRF apparent in Fig. 2a occur at 0.37 and 0.59 COD values, again respectively.

227 Similar forcing profiles have been reported in previous regional studies (e.g., Fig. 13b in  
228 Ackerman et al. 1988; Fig. 3 in Jensen et al. 1994; Fig. 12b in Berry and Mace 2014). Given that

229 each of those studies was in the tropics and mostly over water however, and in the case of Jensen  
230 et al. (1994) and Berry and Mace (2014) reflect diurnal means where night and day are averaged  
231 together, differences seen between those profiles and the ones here are predominantly a  
232 reflection of being daytime profiles alone solved for midlatitude cirrus over land. How such  
233 differences are manifested in the results is discussed further in Sec. 2.4.

234 Shown in Fig. 3 are histograms of cirrus cloud relative frequency and net daytime TOA CRF  
235 normalized by corresponding frequency at GSFC, again for both 20 and 30 sr solutions at 0.03  
236 COD resolution between 0.00 and 3.00 (Figs. 3a and b) and at 0.01 COD resolution between  
237 0.00 and 0.10 (Figs. 3c and d). These data are, again, qualitatively similar to that depicted in  
238 Berry and Mace (2014), though COD is the independent variable here as opposed to ice water  
239 path. Unlike the raw forcing relationships depicted in Fig. 2a however, which are the basis for  
240 the classical models described above, after normalizing by relative frequency, the maxima in  
241 positive net daytime TOA CRF (warming) correspond with COD below 0.10 in both solutions.  
242 Again from Fig. 1, 65-80% of the sample (30/20 sr, respectively) corresponds with COD  $\leq 0.30$ ,  
243 which when normalized for in the net daytime TOA CRF relationships more appropriately  
244 resolves the relative warming component of those clouds in an apparent “shift” to lower COD  
245 relative to the unnormalized solutions. Primary crossover points between positive and negative  
246 net daytime TOA CRF occur near 0.35 and 0.70, respectively, at 20 and 30 sr, which is mostly  
247 unchanged from the unnormalized profiles in Fig. 2.

248 Integrated relative net daytime TOA CRF solved from these data are 0.07 and 0.67 W/m<sup>2</sup>,  
249 respectively, at 30 and 20 sr, respectively. This result is based on the 16% absolute frequency of  
250 cirrus observed within the annual GSFC dataset, which again represents a likely undersampling  
251 of cirrus clouds at this site. Midlatitude net cirrus cloud frequencies are likely nearer to 40%,

252 based on Mace et al. (2009). Assuming however that the distribution of relative cloud  
253 frequencies as a function of COD, as depicted Fig. 3b, is reasonably representative despite  
254 undersampling, these results imply a slight positive cirrus net daytime TOA CRF (warming)  
255 annually at GSFC. After normalizing to unity based on this satellite-based frequency estimate,  
256 net daytime TOA CRF forcing is estimated in absolute terms as ranging between 0.03 and 0.27  
257 W/m<sup>2</sup>.

258 Of particular note is the identification of net daytime cooling at the very lowest COD cases  
259 (COD  $\leq$  0.01; Fig. 3d), and a secondary crossover point between positive and negative net  
260 daytime TOA CRF relative to Figs 2a and 3a. Such a result has been hypothesized in Fu-Liou-  
261 Gu modeling sensitivity analysis (Min et al. 2010). Berry and Mace (2014) also report a very  
262 slight negative forcing component at their lowest ice water path values. Their cloud sample  
263 consists of all day/night ice-phase clouds above 10 km resolved with joint CPR/CALIOP  
264 measurements. Though slightly different than the experimental design considered here, the  
265 consistency with their finding is nevertheless compelling. The mechanics of this process relate  
266 to influence on the net TOA CRF solution due to varying and increasing SZA, which is  
267 described in more detail in Sec. 2.4.

268 Based on Fig. 3b, and given the primary COD warming/cooling crossover points near 0.35  
269 and 0.70 for 20 and 30 sr respectively, undersampling due to attenuation and the lack of multi-  
270 layer clouds is most likely affecting the sample of clouds disproportionately at COD values  
271 greater than both thresholds. Such clouds tend toward negative TOA CRF (cooling).  
272 Corresponding net daytime TOA CRF estimates are thus likely biased high as a result. However,  
273 this effect may be offset somewhat by the lack of relatively warm cirrus in the sample (cloud top  
274 temperatures  $> -37^{\circ}$  C), which Sassen and Campbell (2001) and Campbell et al. (2015) speculate

275 are most likely sheared fallstreaks displaced from their parent cloud and thus are presumed  
276 likeliest to correspond with relatively low COD (positive net TOA CRF/warming; given their  
277 warmer nature, however, and thus lower thermal contrast with the surface, it is not absolutely  
278 clear that they would be significant warmers relative to colder portions of the sample). If  
279 multiple scattering is significantly influencing the results, as well, the relative effect would be to  
280 bias COD low and thus net TOA CRF high, which would exacerbate the effects of  
281 undersampling at higher COD.

282 It is ultimately unclear exactly how each of these relative uncertainties is affecting the net  
283 solutions. Given the distinct disproportionality of optically-thin clouds within the sample  
284 compared with previous studies, however, and combined with the uncertainty of multiple  
285 scattering effects, estimates of net daytime TOA CRF reported here are believed likelier to be  
286 biased high relative with the counterbalancing effects within the sample caused by disregarding  
287 warm cirrus. To be clear, though, the net daytime TOA CRF values reported here are strictly  
288 estimates given the constraints of the input data assembled, and presumably within the practical  
289 bounds of the two lidar ratios applied to render cloud extinction. Still, the results are unique,  
290 albeit in a qualified manner, reflecting a methodology designed to render the most practical  
291 estimate currently possible from autonomous ground-based lidar profiling.

292

293 2.4 Daytime TOA Forcing versus Cloud Top Heights/Temperatures and its Latitudinal  
294 Dependence

295 Relative frequencies of daytime cirrus cloud occurrence as a function of SZA in 1° intervals  
296 and their corresponding normalized net TOA CRF are shown in Figs. 4a and b, respectively. A  
297 crossover point between net positive (warming) and negative (cooling) is found near 55° in both

298 the 20 and 30 sr solutions. Cloud occurrence corresponds most frequently with relatively higher  
299 SZA and negative net forcing. Despite the slightly-positive net integrated daytime TOA CRF  
300 estimated above, normalized net TOA CRF per degree is generally greater at higher relative  
301 SZA. This indicates that the magnitude of single cooling events is generally stronger than that of  
302 warming cases observed at lower SZA.

303 The basis for restricting daytime hours in this study to those where incoming net TOA clear-  
304 sky solar radiation exceeds outgoing total energy is borne out in Fig. 4b. As SZA increases  
305 toward  $80^\circ$ , which proves the approximate effective annual SZA threshold found applying the  
306 definition to these data, mean net daytime TOA CRF gradually converges from negative (i.e.,  
307 cooling) toward zero. It eventually becomes strongly positive (i.e., warming; not shown), under  
308 what are defined as nighttime conditions. As described above, as incoming solar radiation  
309 lessens with increasing solar angle, near the point where total incoming energy equals that  
310 outgoing the solution for net daytime TOA CRF can never turn negative (again, with slight  
311 caveats due to SZA, COD and the thermodynamic profile, though the data shown in Fig. 4b  
312 verify that this offset is mostly negligible) and all clouds become TOA warming elements.  
313 Therefore, the approximated threshold is applied as the only practical means for isolating the  
314 potential fluctuation in the sign of net daytime cirrus cloud TOA CRF, which can only occur  
315 under relatively significant solar insolation during daytime hours. Critically, previous attempts  
316 to reconcile cirrus net TOA CRF properties have considered only the diurnal mean value (e.g.,  
317 Fig. 4 in Fu et al., 2002), as opposed to isolating the specific attributes exhibited by cirrus under  
318 solar illumination.

319 The impact of increasing SZA on net daytime TOA CRF is to enhance cloud solar extinction  
320 relative to thermal effects. As SZA deviates from  $0^\circ$ , the propagation angle of incoming solar

321 energy incident at cloud top changes while thermal emissions below and within the cloud remain  
322 effectively oriented in the zenith/nadir plane. Therefore as SZA increases, the effective solar  
323 COD increases by extending the propagation length within a cloud, increasing relative scattering  
324 (i.e., Beer's Law; Sun et al. 2011 infer a similar effect) and the net solar forcing component  
325 relative to an effectively static thermal one. As seen in Fig. 2b, however, at relatively low COD  
326 this change in effective solar COD can influence the sign of the net solution relating solar and  
327 infrared forcing. Ackerman et al. (1988) and Fu et al. (1993) imply that the relationship is  
328 otherwise always positive, given a reasonably low SZA and for a common range of effective  
329 particle sizes. At relatively high SZA, however, as relative solar COD increases, the sensitivity  
330 of the relationship is such that the sign can reverse. Net daytime TOA CRF near COD = 0.01  
331 depicted in Fig. 2b reflects such reversal in the aggregate, which is the point of enlarging the  
332 scale in that figure relative to Fig. 2a and likely an important consideration as to why previous  
333 researchers, Min et al. (2010) aside (though one has to look very carefully at their result to  
334 resolve it), have not recognized this process.

335 It is critical, though, to recognize that SZA frequency distributions vary with latitude and  
336 season, compared with that solved annually here for this single midlatitude site. Therefore, the  
337 distinct relationship between the sign of net daytime TOA cirrus cloud forcing and SZA in this  
338 analysis implies that a latitudinal variation in net daytime TOA CRF exists globally. Min et al.  
339 (2010) conceptualize how the combination of fluctuating regional surface albedo and variation in  
340 mean macrophysical cirrus cloud properties found with latitude could influence the relative  
341 distribution of positive and negative daytime cirrus TOA CRF relative to SZA. The results here  
342 are the first evidence, however, of how such variance is reflected in actual observations.

343       The frequency of cloud occurrence for relatively high SZA ( $> 55^\circ$ ) increases moving  
344 poleward, which will presumably lead to gradually greater relative net daytime cloud cooling.  
345       Further, lowering mean cloud heights toward the poles and less thermal contrast between the  
346 clouds and surface would suppress the positive relative infrared forcing term (Corti and Peter  
347 2009), as would the impact of offsetting cooling by the very lowest COD layers that would also  
348 increase in significance given the greater frequency of higher SZA cases. The scenario would  
349 then reverse moving from the midlatitudes toward the equator, leading to greater relative positive  
350 daytime forcing (warming) there. Similarly, the primary crossover COD threshold at higher  
351 values, above which negative net TOA solar forcing exceeds the positive infrared component and  
352 clouds become net daytime cooling agents, will be suppressed/enhanced by higher/lower mean  
353 effective SZA for a given site, which will also significantly influence net daytime TOA CRF  
354 values.

355       In winter, high surface albedos over ice and snow and lesser daylight hours available will  
356 offset many of these factors approaching the seasonal pole (higher albedos induce a greater  
357 positive relative solar daytime TOA CRF component, and are thus consistent with greater net  
358 positive daytime TOA CRF overall; Min et al. 2010). During summer, though, as ice and snow-  
359 covered regions retreat, and considering greater daytime hours available relative to polar night  
360 combined with endemically higher SZA, a significant meridional gradient in net daytime cirrus  
361 cloud forcing between warming at the equator and likely cooling near the corresponding pole  
362 likely occurs. The slightly positive forcing value solved at this midlatitude site would thus  
363 represent a location nearing the approximate midpoint along this hypothetical gradient. Further,  
364 given the increase in relative surface albedo over oceans at low SZA (Jin et al. 2004), warming is  
365 likely enhanced even further near the equator, which exacerbates this scenario. Most fascinating

366 about this potential feedback mechanism, though, is its apparent paradoxical nature. If present,  
367 positive/negative daytime cirrus TOA CRF would reinforce warming/cooling near the  
368 equator/summer pole. This, in turn, would act to strengthen meridional temperature gradients,  
369 and thus baroclinicity, most prominently in the summer hemisphere when ice coverage and  
370 nighttime hours are at seasonal minimums.

371 Variability in ice microphysical properties with latitude and season will prove a unique  
372 consideration when evaluating the merits of this hypothesis in future work. For instance, Liou et  
373 al. (2008) describe field measurements that imply distinct latitudinal variability in effective  
374 particle diameter as a function of ice water path. FLG, in fact, features settings that allow the  
375 user to vary this relationship within the model. The Heymsfield et al. (2014) parameterization  
376 relating lidar extinction with ice water content, effective particle diameter and cloud temperature  
377 built into FLG for this study, however, is based on the premise that many field measurements of  
378 ice microphysical properties suffer from sampling bias, induced by shattering of crystals on the  
379 inlets of the instruments designed to measure them. Instead, their parameterization is latitude-  
380 neutral, thus reconciling all apparent hemispheric variability between those three dependent  
381 parameters. Endemic differences in single-scattering properties induced by meridional ice  
382 microphysical variability would influence how net daytime TOA CRF is distributed, however,  
383 and therefore must be considered. Still, with respect to Liou et al. (2008), they suggest solar  
384 cloud albedo near the poles at a relative maximum compared with midlatitudes and tropical  
385 clouds, which, if true (notwithstanding the concerns outlined in Heymsfield et al. [2014]), would  
386 likely exacerbate the proposed gradient further (i.e., greater cooling).

387 The remaining consideration in this paradigm, then, is the mean distribution of cirrus cloud  
388 heights and their sensitivity to net daytime TOA CRF. Shown in Fig. 5, similar to Fig. 4, is the

frequency of cloud top heights in 2012 at GSFC as a function of temperature ( $^{\circ}$  C) in half-degree intervals and the corresponding frequency-normalized net daytime TOA CRF. Infrared CRF is a direct function of the difference in surface temperature and blackbody emissions temperature of the overlying cloud (e.g., Corti and Peter 2009). Therefore, the coldest clouds correspond with the greatest thermal forcing and a positive (warming) daytime TOA CRF overall. A singular crossover point between net warming and cooling occurs near  $-48^{\circ}$  C. Whereas the relative frequency of cloud occurrence increases for colder temperatures, a resulting distribution that is broadly consistent with that of mid-latitude cirrus clouds reported in Campbell et al. (2015) from CALIOP observations, cloud cooling is still relatively significant for the warmer cases. Moving poleward, mean cloud heights decrease as does the thermal contrast between clouds and the surface. During summer months when snow and ice ground cover again retreats, lowering relative surface albedos, this distribution will very likely skew toward greater negative net daytime TOA CRF. The opposite would then be expected moving toward the equator, with greater warming and positive net daytime TOA CRF apparent.

403

### 404 **3. Conclusions**

405 Perhaps the most important contribution made by autonomous lidar monitoring projects, like  
406 MPLNET and CALIOP, to furthering our understanding of global cloud physical processes over  
407 the last decade is the recognition that optically-thin cirrus clouds (cloud optical depths  $< 0.3$ ;  
408 Sassen and Cho 1992) are the most common cloud type in the earth-atmosphere system (e.g.,  
409 Mace et al. 2009; Stubenrauch et al. 2013). Cirrus clouds represent the last tropospheric barrier  
410 to water vapor escaping the hydrologic cycle, and can thus be found over all global regions  
411 during all seasons. Their significance to climate and radiative balance, despite episodic net top-

412 of-atmosphere (TOA) cloud radiative forcing (CRF) values generally on the order of only 1-10  
413 W/m<sup>2</sup> as compared with liquid water clouds that exert TOA CRF on the order of 100 W/m<sup>2</sup>, is  
414 grounded in the long-term aggregate, enhanced by their relatively high occurrence rate and  
415 global extent. This fundamental relationship has been recently illustrated by Berry and Mace  
416 (2014). With increasingly long-term observations of cirrus clouds globally made possible by  
417 continuous ground and satellite-based lidar monitoring, the goal of accurately constraining  
418 seasonal and annual cirrus net daytime and diurnal TOA CRF is increasingly achievable, which  
419 will yield a better understanding of the role cirrus play in cloud radiative budgets overall.

420 In this paper, one-year (2012) of continuously-running NASA MPLNET 532 nm ground-  
421 based lidar observations of single-layer cirrus clouds collected at the NASA Goddard Space  
422 Flight Center (GSFC) are investigated for top-of-atmosphere (TOA) annual net daytime cloud  
423 radiative forcing properties. A slight positive annual net daytime TOA CRF is estimated,  
424 varying between approximately 0.07 and 0.67 W/m<sup>2</sup> in relative terms and 0.03 and 0.27 W/m<sup>2</sup> in  
425 absolute terms. The latter result is reached after normalizing the relative estimate based on a  
426 satellite-approximated 40% midlatitude cirrus cloud occurrence frequency. The methodology  
427 features bookend solutions for cloud extinction estimated from the elastic lidar observations  
428 available (20 and 30 sr settings for the so-called “lidar ratio”) in order to initialize the Fu-Liou-  
429 Gu radiative transfer model. Estimate uncertainties arise from undersampling of relatively high  
430 cloud optical depth (COD) cases, a lack of multi-layer cloud scenes, sample limits for cirrus to  
431 clouds with top height temperatures  $\leq -37^{\circ}$  C and the unresolved impact of laser multiple  
432 scattering. Therefore, these values are strictly estimates of net daytime cirrus TOA CRF at this  
433 site, with the bounds of the lidar ratio settings chosen broadly to approximate any system  
434 variance encountered. This work represents the first known attempt to specifically distinguish

435 daytime cirrus net TOA CRF, applying a specific definition for daytime that isolates the potential  
436 fluctuation in net daytime TOA CRF sign that can only occur when clouds are illuminated by  
437 solar radiance above a threshold roughly equal to clear-sky outgoing energy.

438 Specific features of the annual daytime TOA CRF relationship are highlighted in the  
439 analysis. From the very thinnest clouds ( $COD \leq 0.01$ ), a net negative daytime TOA CRF  
440 (cooling) is identified. Given that relative cloud frequencies are very high in the sample at these  
441 extremely low optical depths, there is some consequential offsetting of bulk warming occurring  
442 from optically-thin clouds that impacts the annual net total. This process is attributed to  
443 relatively high solar zenith angles, and increasing effective solar optical depths relative to  
444 thermal cloud absorption and emissions that remain effectively oriented in the zenith/nadir  
445 planes. For the relatively low solar and infrared TOA CRF values occurring within these clouds  
446 at such low COD, the effect is enough to turn the net solution negative in the aggregate.

447 A distinct relationship between net positive/negative daytime TOA CRF is also demonstrated  
448 as a function of solar zenith angle and cloud top temperature (a proxy in this context for height).  
449 Combined with the influence of surface albedo on TOA CRF, the results at GSFC are used to  
450 conceptualize how cloud forcing likely varies with latitude and season, with cirrus clouds  
451 hypothesized as being net TOA daytime warming elements at the equator, consistent with  
452 existing models, to gradually exerting less positive forcing, and likely a net TOA daytime  
453 cooling, approaching the poles. Consequentially, the slightly positive value estimated at this  
454 midlatitude site is believed to represent a point nearing the middle of such a hypothetical  
455 meridional gradient. The gradient effect is likely strongest in the summer hemisphere, from  
456 lesser relative surface albedos, and more daylight hours and high solar zenith angles (SZA)  
457 nearing the poles combined with low SZA near the equator that enhances surface albedo over

458 open waters and increases TOA warming. It is unclear to what degree meridional variability in  
459 ice microphysical properties may influence this process.

460 Such a gradient, if proven true, would reflect the discovery of a fundamental atmospheric  
461 feedback mechanism that acts to increase hemispheric thermal gradients and baroclinicity. In the  
462 summer hemisphere, when such gradients are seasonally relaxed compared with winter, this  
463 progressive forcing mechanism would represent a significant new process to resolve within  
464 global climate simulations. Most prominently, however, is the binding characteristic that cirrus  
465 clouds are the only cloud genus that can yield a positive net daytime TOA CRF in the first place.  
466 A fluctuating meridional forcing gradient, as such, would be a wholly unique atmospheric  
467 process alone in that context. This potential finding thus represents a fundamentally new way of  
468 considering how cirrus clouds impact TOA energy budgets overall.

469 This work further reinforces how classical conceptual models for cirrus cloud TOA CRF  
470 estimates are based on an antiquated understanding of the physical properties and global  
471 distribution of cirrus clouds, which overemphasize the impact of optically-denser clouds.  
472 Evidence has long mounted raising question as to how these models were manifested globally.  
473 For instance, Stephens et al. (1990) identify a lower threshold in effective cloud particle size  
474 whereby the relationship reverses, and cloud solar reflection exceeds infrared warming at much  
475 lower optical depths than believed common. Khvorostyanov and Sassen (2002) describe three  
476 modeling scenarios for mid-latitude cirrus cloud occurrence, finding a net daytime cloud cooling  
477 in all three cases. Barja and Antuna (2011) report similar results in a limited lidar cloud sample  
478 over Cuba. Here, and on the heels of the work of Berry and Mace (2014) in Southeast Asia, the  
479 impact of relative cirrus cloud frequencies that skew heavily to optically-thin clouds is more  
480 appropriately considered. This analysis thus further develops a foundational basis for

481 extrapolating these results, and the processes resolved, to the global scale, with demonstrable  
482 hypotheses on how global daytime net cirrus TOA CRF varies with latitude and season and what  
483 impact daytime cirrus have to the climate radiation budget as a whole.

484 On one final point comes about from the sustained importance of ground-based profiling of  
485 cirrus clouds, in spite of the ever-burgeoning satellite era anchored currently by CALIOP and in  
486 anticipation of additional future missions. Ground-based observations continue providing  
487 critical satellite ground-truth, albeit with caveats. Most importantly, though, they continue  
488 providing diurnal observations. This study demonstrates specifically how SZA influences  
489 solutions for cirrus net daytime TOA CRF, for instance. Though Min et al. (2010) attempt to  
490 circumvent this aspect of the sun-synchronous CALIOP dataset in a similar study of cirrus cloud  
491 radiative properties, the role for continuous ground-based remote sensing remains clearly defined  
492 in this context. As Thorsen et al. (2011) and Protat et al. (2014) have demonstrated, whereas  
493 ground-based lidar profiling is subject to observational bias (due to attenuation limits caused  
494 mostly by low-level liquid water clouds, but also by thicker cirrus themselves), there remains  
495 significant information content in long-term ground-based datasets for providing regional context  
496 fundamental to reconciling satellite measurements. With hopes of quantifying the global,  
497 regional, annual, seasonal and even diurnal distribution of cirrus net TOA CRF, looking forward  
498 to a study similar to this based on CALIOP datasets, the synergy between ground and satellite  
499 observation should be leveraged to best constrain uncertainties and render the most accurate  
500 result currently possible.

501

502

## ACKNOWLEDGEMENTS

503 The NASA Micro Pulse Lidar Network (MPLNET) is supported by the NASA Radiation

504 Sciences Program (H. Maring). Author JRC acknowledges the support of NASA Interagency

505 Agreement NNG13HH10I on behalf of MPLNET.

506

507

**REFERENCES**

- 508 Ackerman, T. P., K.-N. Liou, F. P. J. Valero, and L. Pfister, 1988: Heating rates in tropical  
509 anvils. *J. Atmos. Sci.*, **45**, 1606–1623.
- 510 Barja, B., and J. C. Antuna, 2011: The effect of optically-thin cirrus clouds on solar radiation in  
511 Camagüey, Cuba. *Atmos. Chem. Phys.*, **11**, 8625-8634, doi:10.5194/acp-11-8625-2011.
- 512 Berry, E., and G. G. Mace, 2014: Cloud properties and radiative effects of the Asian summer  
513 monsoon derived from A-Train data. *J. Geophys. Res. Atmos.*, **119**,  
514 doi:10.1002/2014JD021458.
- 515 Campbell, J. R., D. L. Hlavka, E. J. Welton, C. J. Flynn, D. D. Turner, J. D. Spinhirne, V. S.  
516 Scott, and I. H. Hwang, 2002: Full-time, eye-safe cloud and aerosol lidar observation at  
517 Atmosphere Radiation Measurement program sites: Instrument and data processing. *J.  
518 Atmos. Oceanic Technol.*, **19**, 431-442.
- 519 Campbell, J. R., K. Sassen and E. J. Welton, 2008: Elevated cloud and aerosol layer retrievals  
520 from micropulse lidar signal profiles, *J. Atmos. Oceanic Technol.*, **25**, 685-700.
- 521 Campbell, J. R., Vaughan, M. A., Oo, M., Holz, R. E., Lewis, J. R., and Welton, E. J., 2015:  
522 Distinguishing cirrus cloud presence in autonomous lidar measurements, *Atmos. Meas. Tech.*,  
523 8, 435-449, doi:10.5194/amt-8-435-2015.
- 524 Chew, B. N., J. R. Campbell, J. S. Reid, D. M. Giles, E. J. Welton, S. V. Salinas and S. C. Liew,  
525 2011: Tropical cirrus cloud contamination in sun photometer data, *Atmos. Env.*, **45**, 6724-  
526 6731, doi:10.1016/j.atmosenv.2011.08.017.
- 527 Corti, T., and T. Peter, 2009: A simple model for cloud radiative forcing. *Atmos. Chem. Phys.*, **9**,  
528 5751-5758, www.atmos-chem-phys.net/9/5751/2009/.

- 529 Donovan, D. P., and A. C. A. P. van Lammeren, 2001: Cloud effective particle size and water  
530 content profile retrievals using combined lidar and radar observations 1. Theory and  
531 examples. *J. Geophys. Res.*, **106**, 27,425-27,448.
- 532 Fernald, F.G., 1984: Analysis of atmospheric lidar observations: some comments. *Appl. Opt.*, **23**,  
533 652-653.
- 534 Fu, Q., and K. N. Liou, 1992: On the correlated  $k$ -distribution method for radiative transfer in  
535 nonhomogeneous atmospheres. *J. Atmos. Sci.*, **49**, 2139-2156.
- 536 Fu, Q., and K. N. Liou, 1993: Parameterization of the radiative properties of cirrus clouds. *J.  
537 Atmos. Sci.*, **50**, 2008-2025.
- 538 Fu, Q., K.N. Liou, M. Cribb, T.P. Charlock, and A. Grossman, 1997: Multiple scattering  
539 parameterization in thermal infrared radiative transfer. *J. Atmos. Sci.*, **54**, 2799-2812.
- 540 Fu, Q., M. Baker, and D. L. Hartman, 2002: Tropical cirrus and water vapor: an effective Earth  
541 infrared iris feedback? *Atmos. Chem. Phys.*, **2**, 31-37, [www.atmos-chem-phys.org/acp/2/31](http://www.atmos-chem-phys.org/acp/2/31).
- 542 Garnier, A., J. Pelon, M. A. Vaughan, D. M. Winker, C. R. Trepte, and P. Dubuisson, 2015:  
543 Lidar multiple scattering factors inferred from CALIPSO lidar and IIR retrievals of semi-  
544 transparent cirrus cloud optical depths over oceans. *Atmos. Meas. Tech.*, **8**, 2759-2774,  
545 doi:10.5194/amt-8-2759-2015, 2015.
- 546 Gu, Y., J. Farrara, K. N. Liou, and C. R. Mechoso, 2003: Parameterization of cloud-radiation  
547 processes in the UCLA general circulation model. *J. Climate.*, **16**, 3357-3370.
- 548 Gu, Y., K. N. Liou, S. C. Ou, and R. Fovell, 2011: Cirrus cloud simulations using WRF with  
549 improved radiation parameterization and increased vertical resolution. *J. Geophys. Res.*, **116**,  
550 D06119, doi:10.1029/2010JD014574.

- 551 Heymsfield, A., D. Winker, M. Avery, M. Vaughan, G. Diskin, M. Deng, V. Mitev, and R.  
552 Matthey, 2014: Relationships between ice water content and volume extinction coefficient  
553 from in situ observations for temperatures from 0° to –86°C: Implications for spaceborne  
554 lidar retrievals. *J. Appl. Meteor. Climatol.*, **53**, 479–505.
- 555 Holz, R. E., S. A. Ackerman, F. W. Nagle, R. Frey, S. Dutcher, R. E. Kuehn, M. A. Vaughan,  
556 and B. Baum, 2008: Global Moderate Resolution Imaging Spectroradiometer (MODIS) cloud  
557 detection and height evaluation using CALIOP. *J. Geophys. Res.*, **113**, D00A19,  
558 doi:10.1029/2008JD009837.
- 559 Jensen, E. J., S. Kinne, and O. B. Toon, 1994: Tropical cirrus cloud radiative forcing: Sensitivity  
560 studies. *Geophys. Res. Lett.*, **21**, 2023-2026.
- 561 Jin, M., and S. Liang, 2006: An improved land surface emissivity parameter for land surface  
562 models using global remote sensing observations. *J. Climate*, **19**, 2867-2881.
- 563 Jin, Z., T. P. Charlock, W. L. Smith Jr., and K. Rutledge, 2004: A parameterization of ocean  
564 surface albedo. *Geophys. Res. Lett.*, **31**, L22301, doi:10.1029/2004GL021180.
- 565 Khvorosyanov, V. I., and K. Sassen, 2002: Microphysical processes in cirrus and their impact on  
566 radiation, in: *Cirrus*, edited by: Lynch, D. K., Sassen, K., O'C. Starr, D., and Stephens, G.,  
567 Oxford University Press, New York, 480 pp.
- 568 Lewis, J. R., J. R. Campbell, P. C. Haftings and E. J. Welton, 2016: Overview and analysis of the  
569 MPLNET Version 3 cloud detection algorithm. *J. Atmos. Oceanic Technol.*, revised.
- 570 Liou, K.-N., 1986: The influence of cirrus on weather and climate processes: A global  
571 perspective. *Mon. Wea. Rev.*, **114**, 1167–1199.
- 572 Liou, K.N., Q. Fu, and T.P. Ackerman, 1988: A simple formulation of the delta-four-stream  
573 approximation for radiative transfer parameterizations. *J. Atmos. Sci.*, **45**, 1940-1947.

- 574 Liou, K. N., Y. Gu, Q. Yue, and G. McFarquhar, 2008: On the correlation between ice water  
575 content and ice crystal size and its application to radiative transfer and general circulation  
576 models. *Geophys. Res. Lett.*, **35**, L13805, doi:10.1029/2008GL033918.
- 577 Mace, G. G., Q. Zhang, M. Vaughan, R. Marchand, G. Stephens, C. Trepte, and D. Winker,  
578 2009: A description of hydrometeor layer occurrence statistics derived from the first year of  
579 merged Cloudsat and CALIPSO data. *J. Geophys. Res.*, **114**, D00A26,  
580 doi:10.1029/2007JD009755.
- 581 Min, M., P. Wang, J. R. Campbell, X. Zong, and Y. Li, 2010: Midlatitude cirrus cloud radiative  
582 forcing over China. *J. Geophys. Res.*, **115**, D20210, doi:10.1029/2010JD014161.
- 583 Protat, A., S. A. Young, S. A. McFarlane, T. L'Ecuyer, G. G. Mace, J. M. Comstock, C. N.  
584 Long, E. Berry, and J. Delanoë, 2014: Reconciling ground-based and space-based estimates  
585 of the frequency of occurrence and radiative effect of clouds around Darwin, Australia. *J.*  
586 *Appl. Meteorol. Clim.*, **53**, 456-478, DOI: 10.1175/JAMC-D-13-072.1.
- 587 Sassen, K., and B. S. Cho, B. S., 1992: Subvisual-thin cirrus lidar dataset for satellite verification  
588 and climatological research. *J. Appl. Meteor.*, **31**, 1275–1285.
- 589 Sassen, K., and J. R. Campbell, 2001: A midlatitude cirrus cloud climatology from the Facility  
590 for Atmospheric Remote Sensing Part I: macrophysical and synoptic properties. *J. Atmos.*  
591 *Sci.*, **58**, 481-496.
- 592 Stephens, G. L., and P. J. Webster, 1981: Clouds and climate: Sensitivity of simple systems. *J.*  
593 *Atmos. Sci.*, **38**, 235-247.
- 594 Stephens, G. L., S.-C. Tsay, P. W. Stackhouse Jr., and P. J. Flatau, 1990: The relevance of the  
595 microphysical and radiative properties of cirrus clouds to climate and climatic feedback. *J.*  
596 *Atmos. Sci.*, **47**, 1742-1753.

- 597 Stephens, G. L., D. G. Vane, R. J. Boain, G. G. Mace, K. Sassen, Z. Wang, A. J. Illingsworth, E.  
598 J. O'Connor, W. B. Rossow, S. L. Durden, S. D. Miller, R. T. Austin, A. Benedetti, and C.  
599 Mitrescu, 2002: The Cloudsat mission and the A-Train. *Bull. Amer. Meteorol. Soc.*, **83**,  
600 1771–1790.
- 601 Strahler, A. H., C. B. Schaaf, J.-P. Muller, W. Warmer, M. J. Barnsley, R. d'Entremont, B. Hu, P.  
602 Lewis, X. Li, and E. V. Ruiz de Lope, 1999: MODIS BRDF/albedo product: Algorithm  
603 theoretical basis document. NASA EOS-MODIS Doc. ATBD-MOD-09, version 5.0.
- 604 Stubenrauch, C. J., W. B. Rossow, S. Kinne, S. Ackerman, G. Cesana, H. Chepfer, L. Di  
605 Girolamo, B. Getzewich, A. Guignard, A. Heidinger, b. C. Maddux, W. P. Menzel, P.  
606 Minnis, C. Pearl, S. Platnick, C. Poulsen, J. Riedl, S. Sun-Mack, A. Walther, D. Winker, S.  
607 Zeng, and G. Zhao, 2013: Assessment of global cloud datasets from satellites. *Bull. Amer.*  
608 *Meteorol. Soc.*, **94**, 1031-1049.
- 609 Sun, W., G. Videen, S. Kato, B. Lin, C. Lukashin, and Y. Hu, 2011: A study of subvisual clouds  
610 and their radiation effect with a synergy of CERES, MODIS, CALIPSO, and AIRS data. *J.*  
611 *Geophys. Res.*, **116**, D22207, doi:10.1029/2011JD016422.
- 612 Thorsen, T. J., Q. Fu, and J. Comstock, 2011: Comparison of the CALIPSO satellite and ground-  
613 based observations of cirrus clouds at the ARM TWP sites. *J. Geophys. Res.*, **116**, D21203,  
614 doi:10.1029/2011JD015970.
- 615 Welton, E. J., J. R. Campbell, J. D. Spinhirne, and V. S. Scott, 2001: Global monitoring of  
616 clouds and aerosols using a network of micro-pulse lidar systems, in *Lidar Remote Sensing*  
617 *for Industry and Environmental Monitoring*, U. N. Singh, T. Itabe, and N. Sugimoto, Eds.,  
618 Proc. SPIE, 4153, 151-158.

- 619 Winker, D. M., J. Pelon, J. A. Coakley Jr., S. A. Ackerman, R. J. Charlson, P. R. Colarco, P.  
620 Flamant, Q. Fu, R. Hoff, C. Kittaka, T. L. Kubar, H. LeTreut, M. P. McCormick, G. Megie,  
621 L. Poole, K. Powell, C. Trepte, M. A. Vaughan, and B. A. Wielicki, 2010: the CALIPSO  
622 mission: A global 3D view of aerosols and clouds. *Bull. Amer. Meteorol. Soc.*, **91**, 1211–  
623 1229.
- 624 Yang, P., K. N. Liou, K. Wyser, and D. Mitchell, 2000: Parameterization of the scattering and  
625 absorption properties of individual ice crystals. *J. Geophys. Res.*, **105**, 4699–4718.
- 626 Yang, P., H. Wei, H-L. Huang, B. A. Baum, Y. X. Hu, G. W. Kattawar, M. I. Mishchenko, and Q.  
627 Fu, 2005: Scattering and absorption property database for nonspherical ice particles in the  
628 near- through far-infrared spectral region. *Appl. Opt.*, **44**, 5512–5523.
- 629
- 630

631 **Figure Captions**

632

633 **Figure 1** Histograms of daytime cirrus cloud macrophysical properties at the NASA  
634 Goddard Space Flight Center (GSFC) Micro Pulse Lidar Network (MPLNET) site in  
635 2012 solved using 20 and 30 sr constraints for lidar extinction-to-backscatter (S)  
636 respectively. Cloud properties are distinguished as functions of cloud optical depth (COD;  
637  $\leq 0.03$ , blue;  $0.03 < COD \leq 0.30$ , yellow;  $> 0.30$ , red), and include (a, b) cloud top height  
638 in 0.50 km intervals above mean sea level (MSL), (c, d) cloud depth in 0.25 km intervals  
639 and (e, f) cloud top temperature in  $2^{\circ}$  C intervals. Corresponding sample totals and  
640 relative percentages for each optical grouping and S value are included in the  
641 corresponding upper insets.

642

643 **Figure 2** For the 2012 GSFC daytime GSFC cirrus cloud subset, average top-of-  
644 atmosphere (TOA) infrared, shortwave and net cloud radiative forcing (CRF) for (a)  
645 cloud optical depths between 0.0 and 3.0 and (b) cloud optical depths between 0.01 and  
646 0.10, for the 20 sr (blue) and 30 sr (red) S-value solutions respectively.

647

648 **Figure 3** For the 2012 GSFC daytime GSFC cirrus cloud subset, (a) relative frequency of  
649 cloud occurrence versus cloud optical depth (COD) in 0.03 intervals between 0.0 and 3.0,  
650 (b) average net TOA CRF Fig. 2a normalized by relative frequency in (a), again in 0.03  
651 COD intervals between 0.0 and 3.0, and (c and d) corresponding plots in 0.01 COD  
652 intervals between 0.0 and 0.1, for the 20 sr (blue) and 30 sr (red) S-value solutions  
653 respectively.

654

655   **Figure 4**     For the 2012 GSFC daytime GSFC cirrus cloud subset, (a) relative frequency of  
656       cloud occurrence versus solar zenith angle in  $1^\circ$  intervals (see text for specific definition  
657       for daytime hours) and corresponding average net TOA CRF (Fig. 2a) normalized by  
658       these frequencies, for the 20 sr (blue) and 30 sr (red) S-value solutions respectively.

659

660   **Figure 5**     For the 2012 GSFC daytime GSFC cirrus cloud subset, (a) relative frequency of  
661       cloud occurrence versus cloud top temperature in  $0.5^\circ$  C intervals  $\leq -37^\circ$  C (see text for  
662       justification) and corresponding average net TOA CRF (Fig. 2a) normalized by these  
663       frequencies, for the 20 sr (blue) and 30 sr (red) S-value solutions respectively.

664

665

666   **Table Captions**

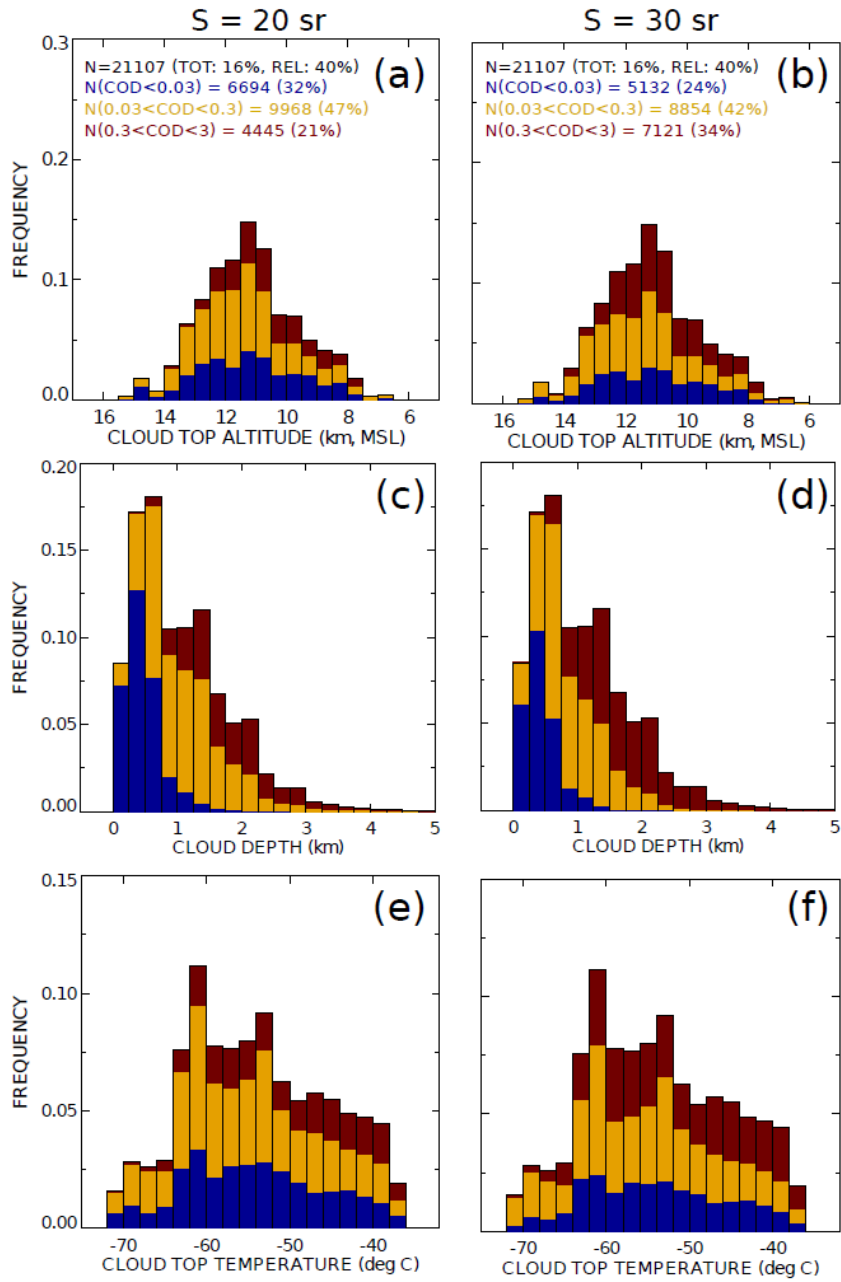
667

668   **Table 1** A summary listing of primary experimental components and constraints used in this  
669       study.

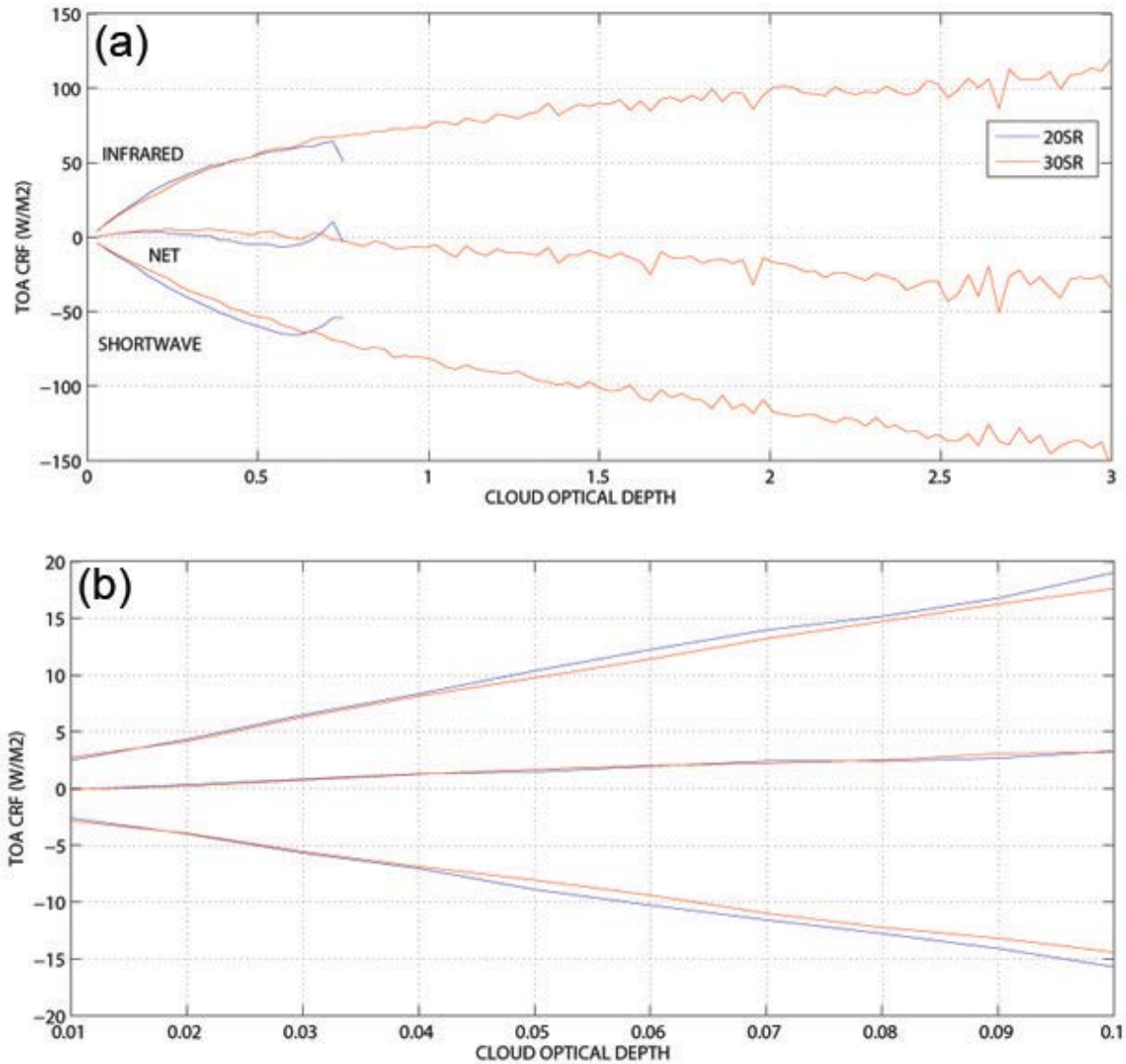
670

671

672

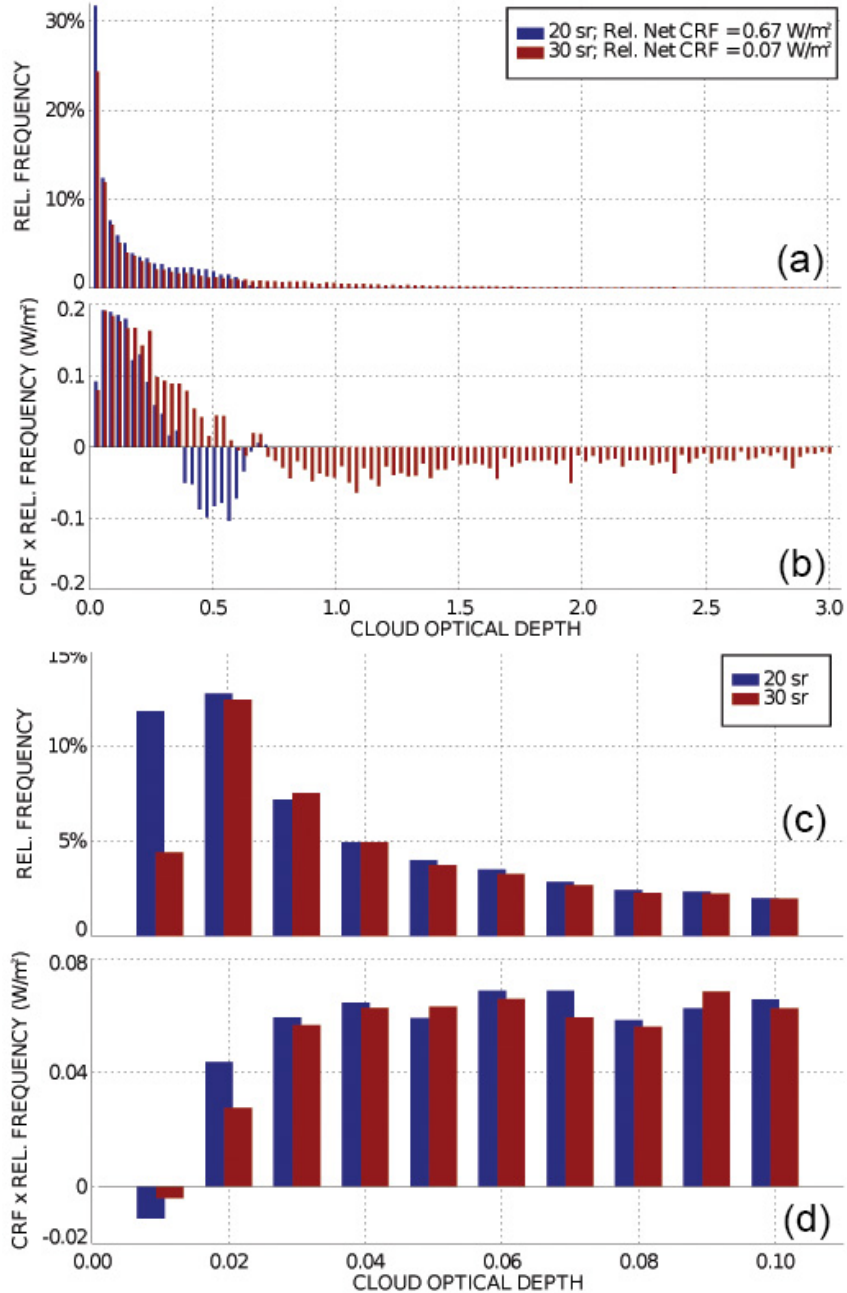
**FIGURE 1**

Histograms of daytime cirrus cloud macrophysical properties at the NASA Goddard Space Flight Center (GSFC) Micro Pulse Lidar Network (MPLNET) site in 2012 solved using 20 and 30 sr constraints for lidar extinction-to-backscatter ( $S$ ) respectively. Cloud properties are distinguished as functions of cloud optical depth (COD;  $\leq 0.03$ , blue;  $0.03 < COD \leq 0.30$ , yellow;  $> 0.30$ , red), and include (a, b) cloud top height in 0.50 km intervals above mean sea level (MSL), (c, d) cloud depth in 0.25 km intervals and (e, f) cloud top temperature in  $2^\circ$  C intervals. Corresponding sample totals and relative percentages for each optical grouping and  $S$  value are included in the corresponding upper insets.



**FIGURE 2**

For the 2012 GSFC daytime GSFC cirrus cloud subset, average top-of-atmosphere (TOA) infrared, shortwave and net cloud radiative forcing (CRF) for (a) cloud optical depths between 0.0 and 3.0 and (b) cloud optical depths between 0.01 and 0.10, for the 20 sr (blue) and 30 sr (red) S-value solutions respectively.

**FIGURE 3**

For the 2012 GSFC daytime GSFC cirrus cloud subset, (a) relative frequency of cloud occurrence versus cloud optical depth (COD) in 0.03 intervals between 0.0 and 3.0, (b) average net TOA CRF Fig. 2a normalized by relative frequency in (a), again in 0.03 COD intervals between 0.0 and 3.0, and (c and d) corresponding plots in 0.01 COD intervals between 0.0 and 0.1, for the 20 sr (blue) and 30 sr (red) S-value solutions respectively.

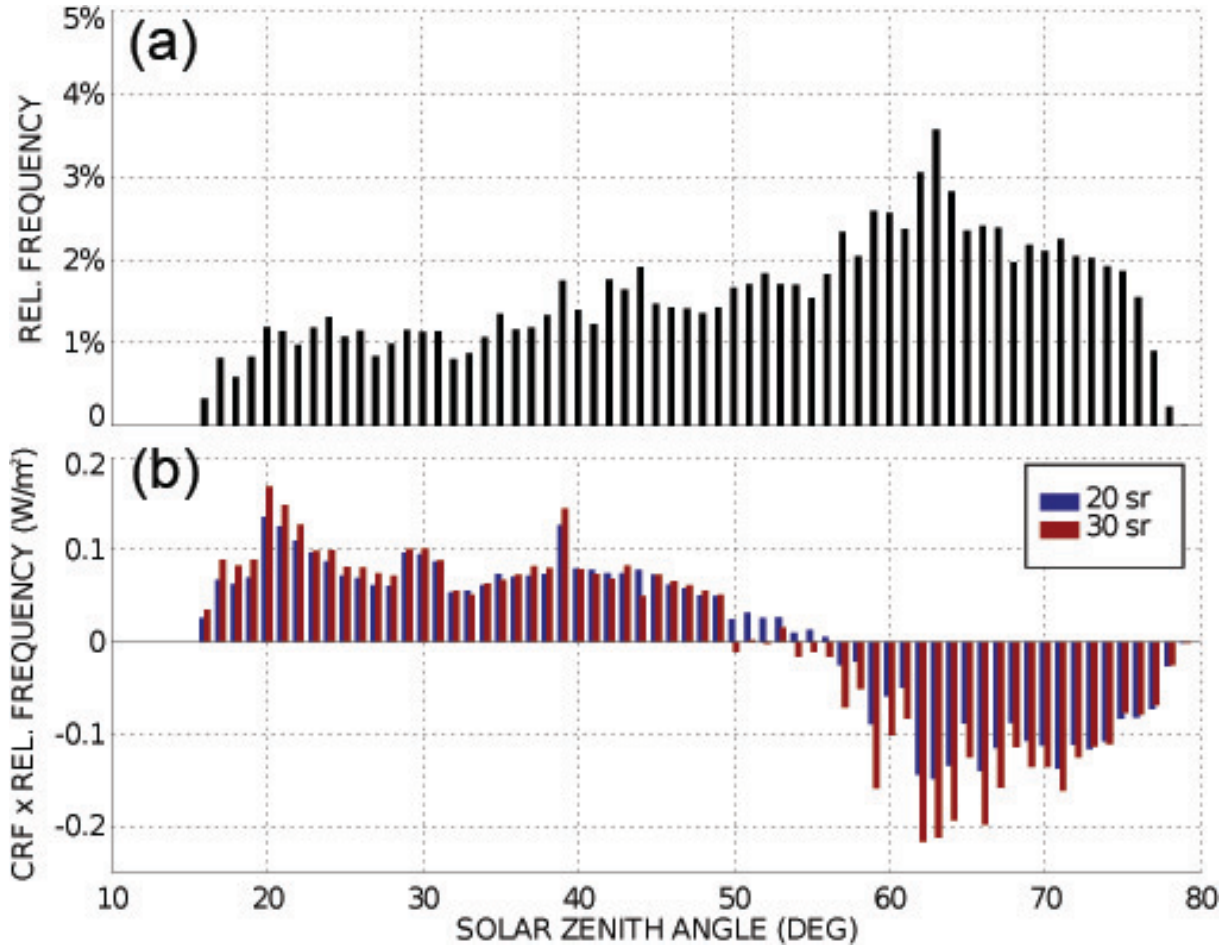


**FIGURE 4**

For the 2012 GSFC daytime GSFC cirrus cloud subset, (a) relative frequency of cloud occurrence versus solar zenith angle in  $1^\circ$  intervals (see text for specific definition for daytime hours) and corresponding average net TOA CRF (Fig. 2a) normalized by these frequencies, for the 20 sr (blue) and 30 sr (red) S-value solutions respectively.

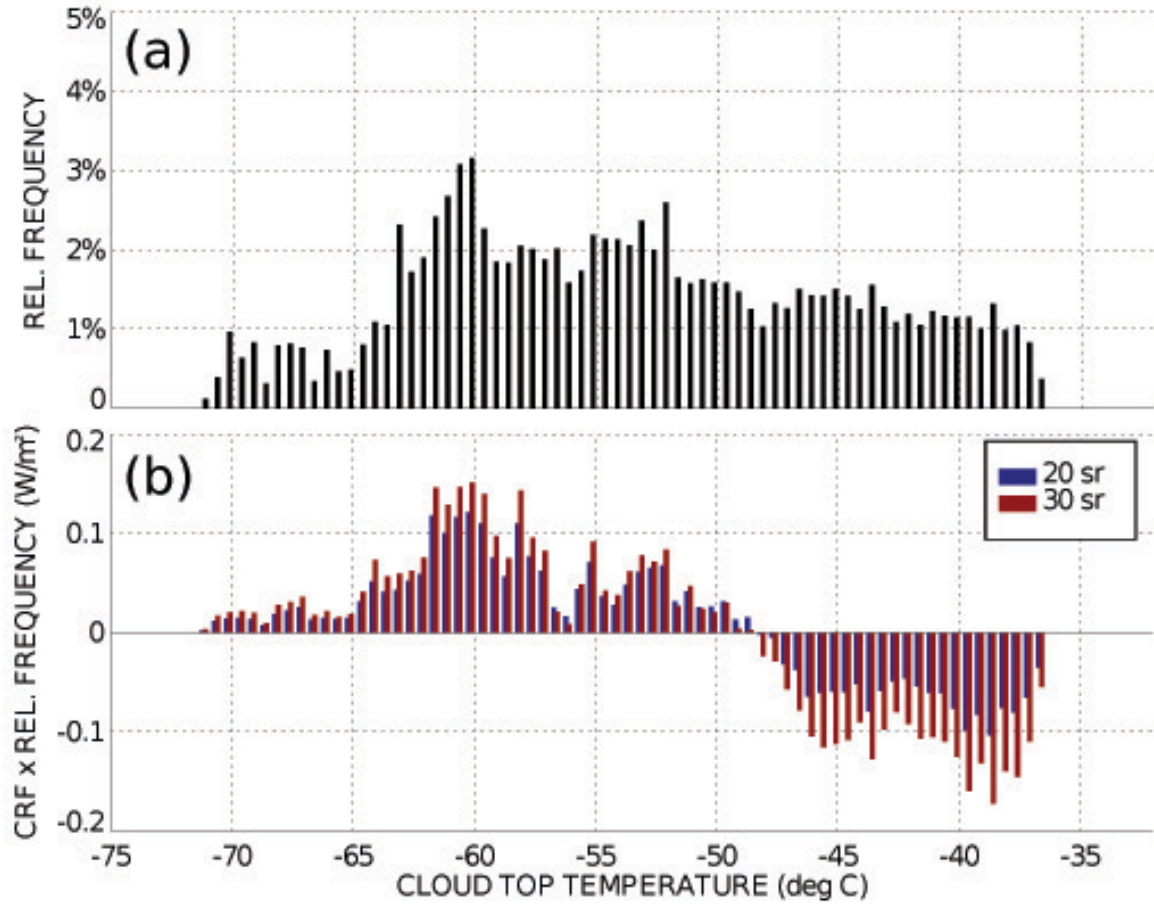


**FIGURE 5**

For the 2012 GSFC daytime GSFC cirrus cloud subset, (a) relative frequency of cloud occurrence versus cloud top temperature in  $0.5^{\circ}$  C intervals  $\leq -37^{\circ}$  C (see text for justification) and corresponding average net TOA CRF (Fig. 2a) normalized by these frequencies, for the 20 sr (blue) and 30 sr (red) S-value solutions respectively.

<b>Experimental Component</b>	<b>Selection</b>	<b>References (<i>if applicable</i>)</b>
Radiative transfer model	Fu-Liou-Gu δ-four stream system	Fu and Liou (1992, 1993); Gu et al. (2003)
Model meteorology	GEOS-5	<a href="http://gmao.gsfc.nasa.gov/products">http://gmao.gsfc.nasa.gov/products</a>
Surface albedo	MODIS monthly-averaged broadband values	Strahler et al. (1999)
Land-surface thermal emissivity	0.97	Jin and Liang (2006)
Ice microphysical parameterization	n/a	Heymsfield et al. (2014)
Definition for daytime hours	Incoming clear-sky top-of-atmosphere solar radiation exceeds outgoing	<i>n/a</i>
Cirrus cloud dataset	MPLNET Version 3.0 cloud product	Campbell et al. (2008); Lewis et al. (2016); <a href="http://mplnet.gsfc.nasa.gov/">http://mplnet.gsfc.nasa.gov/</a>
Cirrus cloud thermal constraints	Cloud top height temperatures $\leq -37^{\circ}$ C	Campbell et al. (2015)

**TABLE 1**

A summary listing of primary experimental components and constraints used in this study.